

An integrated model for materials in a fusion power plant: transmutation, gas production, and helium embrittlement under neutron irradiation

This article has been downloaded from IOPscience. Please scroll down to see the full text article.

2012 Nucl. Fusion 52 083019

(<http://iopscience.iop.org/0029-5515/52/8/083019>)

View [the table of contents for this issue](#), or go to the [journal homepage](#) for more

Download details:

IP Address: 193.52.216.130

The article was downloaded on 13/11/2012 at 13:27

Please note that [terms and conditions apply](#).

An integrated model for materials in a fusion power plant: transmutation, gas production, and helium embrittlement under neutron irradiation

M.R. Gilbert, S.L. Dudarev, S. Zheng, L.W. Packer and J.-Ch. Sublet

EURATOM/CCFE Fusion Association, Culham Centre for Fusion Energy, Abingdon, Oxfordshire OX14 3DB, UK

E-mail: mark.gilbert@ccfe.ac.uk

Received 16 January 2012, accepted for publication 11 July 2012

Published 1 August 2012

Online at stacks.iop.org/NF/52/083019

Abstract

The high-energy, high-intensity neutron fluxes produced by the fusion plasma will have a significant life-limiting impact on reactor components in both experimental and commercial fusion devices. As well as producing defects, the neutrons bombarding the materials initiate nuclear reactions, leading to transmutation of the elemental atoms. Products of many of these reactions are gases, particularly helium, which can cause swelling and embrittlement of materials.

This paper integrates several different computational techniques to produce a comprehensive picture of the response of materials to neutron irradiation, enabling the assessment of structural integrity of components in a fusion power plant. Neutron-transport calculations for a model of the next-step fusion device DEMO reveal the variation in exposure conditions in different components of the vessel, while inventory calculations quantify the associated implications for transmutation and gas production. The helium production rates are then used, in conjunction with a simple model for He-induced grain-boundary embrittlement based on electronic-structure density functional theory calculations, to estimate the timescales for susceptibility to grain-boundary failure in different fusion-relevant materials. There is wide variation in the predicted grain-boundary-failure lifetimes as a function of both microstructure and chemical composition, with some conservative predictions indicating much less than the required lifetime for components in a fusion power plant.

(Some figures may appear in colour only in the online journal)

1. Introduction

In magnetic-confinement fusion devices a large number of high-energy neutrons are generated in the plasma by deuterium–tritium fusion reactions. These neutrons escape from the plasma and irradiate the materials that make up the reactor vessel. One of the key outstanding issues for the fusion materials programme is in the understanding of how neutrons influence the properties of materials over the projected lifetime of a fusion power plant. Not only do the incident neutrons cause atomic displacements within the materials, leading to the generation and accumulation of radiation defects, which cause hardening, embrittlement, and irradiation creep, but they also initiate non-elastic nuclear reactions that alter the nature of the constituent atoms. This process, known as transmutation or burn-up, changes the chemical composition of materials, leading in turn to measurable changes in structural and mechanical properties.

Perhaps even more problematic are the nuclear reactions initiated by fusion neutrons that give rise to the transmutation production of gas atoms, such as helium (He) and hydrogen (H). These reactions, which include neutron capture followed by α -particle (${}^4\text{He}^{2+}$) emission, often written as (n,α) , and neutron capture and proton (${}^1\text{H}^+$) emission (n,p) , generally occur less frequently than the major (n,γ) reactions, but have a much more significant effect on properties of materials, particularly metals and alloys. Even at low concentrations, gas particles can have severe life-limiting consequences for materials, with He being a particular problem because, with its low solubility in the crystal lattice, it forms clusters and accumulates at defects, dislocations and at grain boundaries, leading to swelling or embrittlement.

In fusion, the issue of transmutation gas production is likely to be a more significant problem than in fission because of the higher neutron fluxes and higher average neutron energies. For example, in figure 1 where a fission spectrum

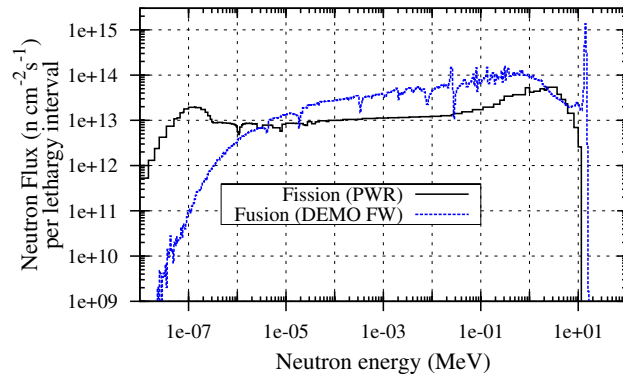


Figure 1. Comparison of the neutron-energy spectra in fission and fusion reactors. For fission the average neutron spectrum in the fuel assembly of a PWR reactor is shown, while the equatorial FW armour spectrum for the DEMO model in figure 2 is representative of fusion.

for a fuel assembly of a 3.8 GW (gigawatts of thermal power) LWR-P4 reactor in Paluel, France, is compared to a fusion spectrum computed for the first wall (FW) armour of the 3.0 GW DEMO concept reactor described later, the fluxes of neutrons per lethargy interval¹ are greater in the fusion spectrum at all but thermal energies. Having said that, the room temperature, homogeneous modelling employed for the DEMO concept does not fully describe the thermal part of the neutron flux, and so in reality the fusion spectrum may also be higher in this region as well. Furthermore, whereas the bulk neutron energy in fission is in the 2 MeV range, for every deuterium–tritium fusion reaction in the plasma a 14.1 MeV neutron is produced.

Many of the gas-producing nuclear reactions exhibit cross section thresholds, which means that for incident neutrons below a particular energy the reaction either does not occur or has a very low probability. Thus, in fusion, while the higher neutron fluxes compared to fission would increase the total number of reactions in irradiated components, the larger fraction of neutrons at higher energies would also tend to raise the proportion of those reactions which lead to helium and hydrogen gas production.

Since experimental testing of materials in a fully realistic fusion neutron-irradiation environment is not currently possible, simulation and theory has a vital role in providing predictions for material response as a result of neutron bombardment and the corresponding build-up of elemental impurities.

This paper gives an example of an integrated approach involving neutron-transport simulations, calculations of the evolution in material composition, and atomic level modelling of the changes to material properties caused by the various aspects of transmutation. For the present study, the last of these three components is only concerned with modelling of helium-induced grain-boundary embrittlement, producing, in combination with knowledge of transmutation response, estimates of the timescales for the loss of structural integrity of

¹ A lethargy interval is a standard measure for spectra of this type, and is equal to the natural logarithm of the ratio of a given energy-interval's upper bound to its lower bound. The total flux in the interval is divided by the resulting value to give flux per lethargy interval, which is plotted in figure 1 and elsewhere as a step function against the interval bounds.

components due to grain-boundary failure. As this integrated approach develops in the future, perhaps with an additional step involving the creation and modification of a reactor's design, other more realistic and relevant models of the consequences of irradiation damage and transmutation could be applied.

The particular strength of this integrated approach is that it allows the variation of radiation effects with position within a particular reactor design to be fully appreciated, and we pay particular attention to this in the paper.

2. Neutron-induced transmutation of materials

In a previous study [1], we considered the transmutation response of various materials under identical FW conditions for both a power plant design (PPCS model B [2]) and for the ITER device, which is presently under construction. While this provided significant insight into the differing behaviour of materials under neutron irradiation, particularly with regard to He/H gas production, it is important to appreciate the limitations of the approach. Specifically, not all the components of a fusion reactor will experience the same flux and spectrum of neutrons as that seen in the FW armour. In fact, the FW environment will be the worst in terms of transmutation and gas production due to the high neutron fluxes and energies, and conditions elsewhere may be significantly different. Below we investigate how the neutron-irradiation characteristics change as a function of position in a recent design for a demonstration fusion power plant ('DEMO') and calculate the implications for transmutation and gas production in the materials relevant to a particular position in the structure.

2.1. Geometry dependence of neutron flux and energy spectrum

Figure 3 shows neutron spectra calculated for different regions of a recent design, developed at CCFE in 2009, for the DEMO reactor, which is planned as the last step after ITER before progression to commercial fusion power generation. This particular design is helium cooled with a Li/Be tritium-breeding blanket and a W divertor. EUROFER is the primary in-vessel structural steel. A model geometry of the design (figure 2) was created using the HERCULES code [3,4], and neutrons were transported through it using the MCNP code [5]. Only the major structures were included in the design, with homogeneous material compositions taken as the average composition of all of the materials present in a particular component. This means that, for example, the helium cooling pipes are not modelled explicitly, but rather helium as a chemical element is included in the overall composition of the surrounding region. This homogeneous approach is often used in neutron-transport ('neutronics') scoping calculations, and is considered accurate in most circumstances. However, once the design of DEMO is specified in greater detail, a fully heterogeneous model can be employed to refine the predictions.

To increase the speed of the calculations and, more specifically, to reduce the time needed to reach statistically converged neutron spectra, the radial symmetry of the vessel was utilized to model only a 90° segment of the vessel

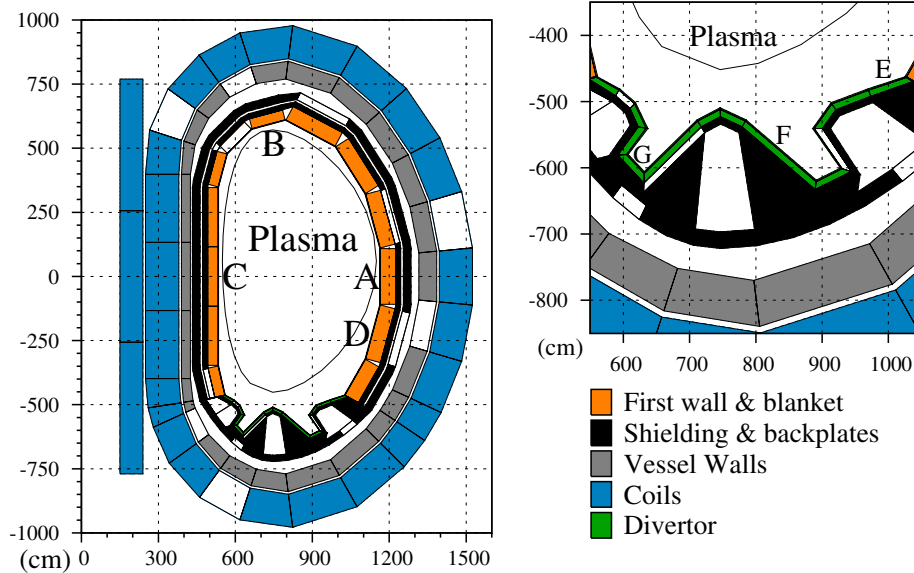


Figure 2. A toroidal section through the simplified, homogeneous, DEMO model used in MCNP simulations to obtain neutron fluxes and spectra.

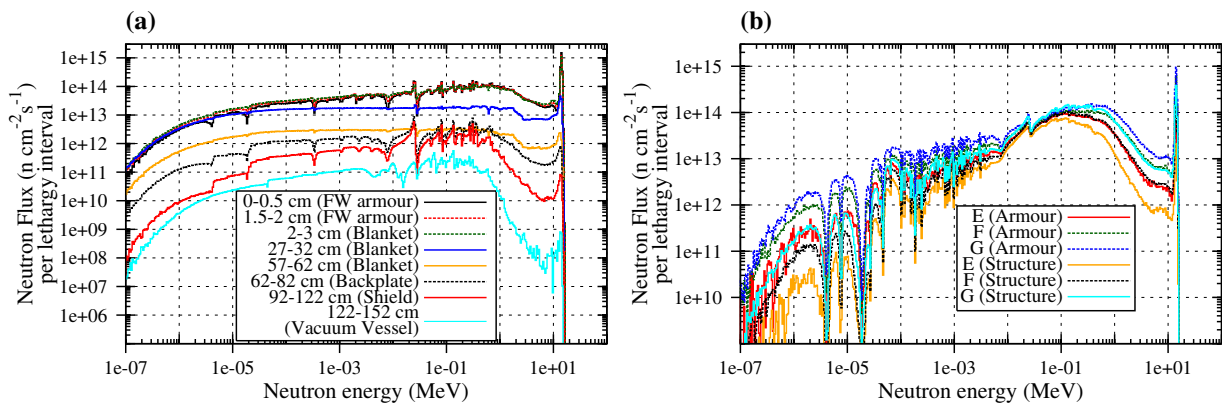


Figure 3. Comparison of the neutron-energy spectra in DEMO; (a) as a function of depth into the vessel from the plasma-facing wall at the equatorial position A in figure 2; and (b) in the first two layers of the divertor as a function of position (E–G in figure 2).

with reflecting planes, and with the neutron fluxes correctly weighted to reflect the fact that only a quarter of the neutron-generating fusion plasma was represented. A sufficient number of neutron trajectories were tracked to obtain adequate sampling of the neutron spectra in the regions of interest. The flux results from MCNP, which are given in units of neutrons per square centimetre (n cm^{-2}) per source neutron n_s , were then multiplied by $9.576 \times 10^{20} n_s \text{ s}^{-1}$ corresponding to the 2.7 GW expected thermal power output from the plasma of DEMO, assuming 17.6 MeV energy output per fusion reaction, producing one 14.1 MeV neutron. Note that extra heat is generated by the exothermic nuclear reactions in the blanket, to give a total of 3.0 GW of thermal power output.

Figure 3(a), which shows the absolute variation in neutron spectra as a function of depth into the equatorial region of the FW armour and beyond (position A in figure 2), demonstrates that both the energy profile and fluxes change dramatically over relatively short distances. For example, the flux at the inner-edge of the blanket region, immediately behind the 2 cm steel armour of the FW, is not very different from the flux in this FW armour. However, as the neutrons pass deeper into

the blanket they become heavily moderated due to the high concentration ($\sim 74\%$) of Be, and thus the neutron spectrum is very different. In turn, this promotes neutron absorption, particularly by ${}^6\text{Li}$ ($\sim 7\%$ in the blanket for tritium breeding). As a result, by the outer edge of the 60 cm thick blanket in this model, situated at a total depth from the plasma-exposed FW armour of 57–62 cm, the flux at most energies has fallen by an order of magnitude or more, and the total flux has dropped from $8.36 \times 10^{14} \text{ n cm}^{-2} \text{ s}^{-1}$ in the first centimetre of the equatorial blanket at position A (at a depth of 2–3 cm), to $3.9 \times 10^{13} \text{ n cm}^{-2} \text{ s}^{-1}$ in the final five cm—a drop of more than 95%.

Within the divertor, on the other hand, the neutron flux and spectrum shows significant variation as a function of position, as well as depth (see figure 3(b)). At point E in figure 2, the total flux in the 2 cm layer of pure W divertor armour and in the 10 cm structural layer behind it, containing 20 wt% cooling He as well as W, is approximately twice as high as that in the same layers at G— $7.1 \times 10^{14} \text{ n cm}^{-2} \text{ s}^{-1}$ and $5.6 \times 10^{14} \text{ n cm}^{-2} \text{ s}^{-1}$ at E in the armour and structure, respectively, versus $3.6 \times 10^{14} \text{ n cm}^{-2} \text{ s}^{-1}$ and $2.4 \times 10^{14} \text{ n cm}^{-2} \text{ s}^{-1}$, respectively at G.

Note that in figure 3(b) the high concentration of W in the divertor causes a visible self-shielding effect in the lower-energy regions of the neutron spectra. The giant resonances in the neutron-capture cross sections of W produce a much-reduced flux at energies below the resonances [1], leading to the troughs in the spectra around 10 eV. In the divertor, this does not cause any undesirable effects, but it could have a significant impact on tritium breeding if too much tungsten, in the form of pure material, say as plasma-facing tiles, or as an alloying component in steel, is used near the blanket because it would suppress, via self-shielding, the population of low-energy neutrons in the blanket that give a significant contribution to tritium breeding. Fortunately, the relatively small self-shielding produced by the 1.1 wt% of W in the EUROFER [6] of the FW armour, which causes the two minor troughs either side of 10 eV in some of the spectra of figure 3(a), is unlikely to have a significant impact on tritium breeding. The effect of tungsten plasma-facing tiles on the spectrum of neutrons reaching the tritium-breeding blanket is not considered here.

As is commonly done to aid interpretation of irradiation conditions, we have also calculated the displacements per atom (dpa) per second corresponding to the neutron spectra and fluxes obtained above. Energy-dependent total dpa cross sections were computed using an early version of the NJOY [7] nuclear data processing system. The product of reaction cross section and the energy transferred to lattice atoms that can produce displacements resulting from the said reaction [8] was summed over all reactions onto the naturally occurring isotopes of each element to give the displacement kerma cross section as a function of incident neutron energy E_n :

$$\sigma_d(E_n) = \sum_j \sigma_j(E_n) E_j(E_n), \quad (1)$$

where σ_j is the collision cross section in barns ($1 \text{ b} = 10^{-24} \text{ cm}^2$) of reaction j taken from the European Fusion File (EFF-1), and E_j is the transferred energy from the reaction at the given energy computed via a modified version of the Lindhard [9] partition function [8]. Using the modified Kinchin-Pease method of Norgett, Robinson, and Torrens [10] (the ‘NRT’ method), the NRT dpa cross section at energy E_n is then calculated in units of NRT dpa·barns as

$$\sigma^{\text{dpa}}(E_n) = \frac{0.8\sigma_d(E_n)}{2E_d}, \quad (2)$$

where E_d is the average displacement energy threshold for production of a Frenkel vacancy-self-interstitial atom defect pair in the bulk of the material. The estimated values of E_d for pure materials used in the present work were 31 eV for Be, 40 eV for Fe, Cr, V, Nb and Zr, 60 eV for Mo and 90 eV for W and Ta [11]. Note that in real fusion components these elements will mainly be present as part of alloys where the threshold displacement energies could be quite different, but for the present the calculations are restricted to the equivalent NRT dpa in pure materials.

For each neutron spectrum and flux, the damage rate expressed in NRT dpa per second was calculated by convoluting the group-wise neutron flux spectrum with the

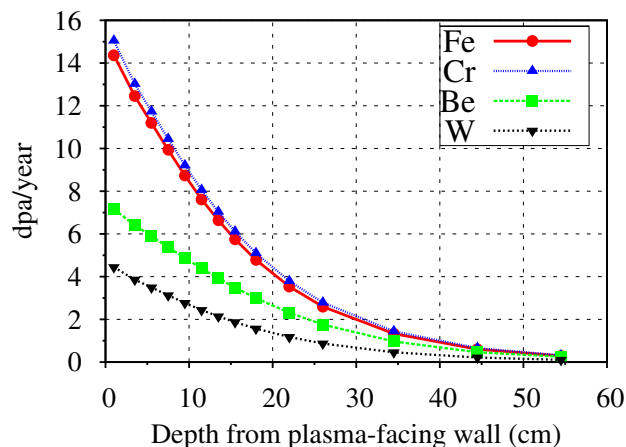


Figure 4. Defect production rates, expressed in dpa per year units for different elements shown as a function of depth into the FW armour and blanket at A in figure 2.

total NRT dpa cross section for a given material computed using an identical neutron-energy group structure:

$$\text{NRT dpa per second} = \sum_i^{N_g} \phi_i \sigma_i^{\text{dpa}}, \quad (3)$$

where N_g is the total number of energy groups (175 for the NRT dpa calculations), ϕ_i is the total flux in group i with units of neutrons $\text{cm}^{-2} \text{ s}^{-1}$, and σ_i^{dpa} is the total NRT dpa cross section for the group.

Here it is important to understand the limitations of the NRT dpa estimates discussed above. The NRT dpa values (referred to subsequently as dpa values) do not take into account the time evolution of radiation damage in the materials, such as recombination, migration, and coalescence of radiation defects, and in this sense are *not* a measure of radiation damage and do not give any direct information about changes in microstructure or to material properties. Instead, they represent an atom-based approximate measure of the irradiation exposure of the material to the fusion neutrons [12].

The resulting dpa per second defect production rate for one material can be quite different to that in another material under the same irradiation conditions because of differences in the cross sections of neutron reactions. For example, figure 4 gives the variation in dpa per year as a function of depth into the FW at A in figure 2 for the main elements considered in this study. Recall, that, for simplicity, here and elsewhere we are only calculating the dpa values that would result from irradiation of pure materials under the chosen neutron spectrum. The defect production dpa/year rate falls off rapidly with depth for all materials, but is significantly higher in Fe and Cr than in either Be or W². For example, in the 2 cm FW armour layer at A, the dpa/year is 14.4, 15.0, 7.2 and 4.4 in Fe, Cr, Be and

² Note that the data used for the dpa calculations presented here, which comes from the European Fusion File (EFF) 1.1, may underestimate the dpa rates for W. Provisional results obtained using more recent and robust nuclear data files and processing sequences suggest that the actual dpa rates in W may be more similar to those obtained for Fe (whose values do not change significantly with the new data files). Since this could have significant engineering implications for W, further work is needed to validate the new results, and so they are not presented here.

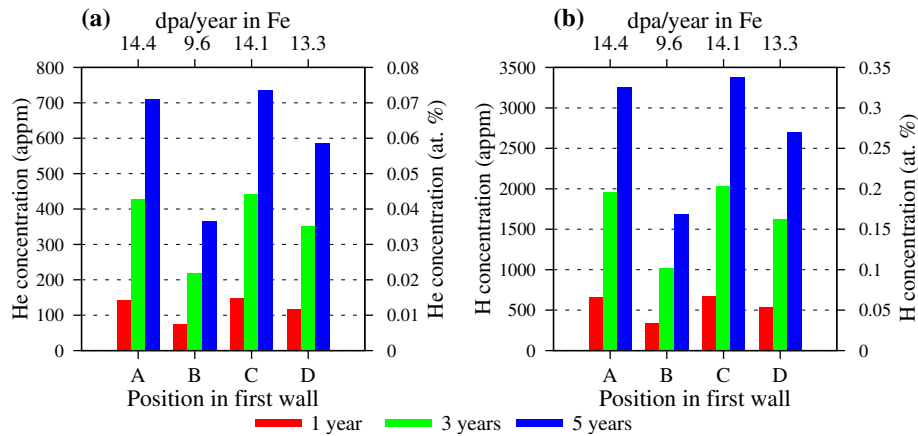


Figure 5. Variation in the (a) He, and (b) H, concentrations in pure Fe as a function of time for the spectra at different FW armour positions in DEMO—see figure 2. The equivalent dpa/year in pure Fe at each position are also given.

W, respectively. Note that the assumption of pure elemental materials for the dpa calculations has a further consequence here—we do not account for the compositional changes, either elemental or isotopic, that take place over time. In reality, even in a pure material the defect production dpa per second rate may change as some of the initial atoms are transmuted. However, under the relatively low burn-up rates explored here, the difference between the dpa rate in the pure material and the mixed composition that is created under irradiation will only be very minimal.

2.2. Influence on transmutation and gas production

The calculated neutron spectra and total fluxes have been used as input to the inventory code FISPACT [13], which simulates both the evolution in activation and the burn-up (transmutation) of different materials under neutron irradiation. FISPACT requires an external library of reaction cross sections, which are *collapsed* (i.e. the vector dot product is taken) with the given neutron spectrum, as well as decay data. For the present work we have employed the 2003 version of the European Activation File (EAF) [14], which is the dedicated library compiled specifically for fusion-relevant calculations with FISPACT.

In the earlier analysis [1] the transmutation of different materials was compared using identical irradiation conditions, which in that case were those expected in the FW of a conceptual power plant. Here, we consider the effect on Fe, W, and Be as function of position in the regions of DEMO where they are most likely to be employed within a fusion reactor. Note that, for W, we employ the self-shielding correction-factors obtained in [1] and apply them to the FISPACT calculations. Other materials, such as Cu and SiC, are present in significant quantities in several power plant concepts (SiC, for example, is often proposed as an alternative FW armour material), but the present calculations are restricted to the three materials that make up the majority of the in-vessel components in the DEMO model investigated here.

2.2.1. Fe. The gas production in bulk Fe, as the major constituent of steels, will be a major factor in determining the lifetime of near-plasma component in fusion reactors, and so deserves special attention. Note that chromium (Cr), which is

likely to represent around 10% of the composition of reduced activation steels being proposed for fusion applications, has a very similar transmutation profile to Fe, and so the gas concentrations levels calculated for pure Fe are a very good match to those expected in such steels.

Figure 5 shows how the concentration of He and H produced under irradiation varies as a function of position in the FW armour of the DEMO model. The irradiation times considered here and elsewhere in this work are full-power years, and no attempt has been made to account for maintenance down-times, and other factors determining the availability of the power plant. The dpa/year rates for pure Fe at each of the four positions have also been calculated. The shapes of the neutron spectra averaged over the 2 cm FW armour at positions A–D in figure 2 are all very similar. However, the total flux in these different regions of the FW armour does vary somewhat, with the total flux being $8.25 \times 10^{14} \text{ n cm}^{-2} \text{ s}^{-1}$ at A, $6.97 \times 10^{14} \text{ n cm}^{-2} \text{ s}^{-1}$ at B, $8.04 \times 10^{14} \text{ n cm}^{-2} \text{ s}^{-1}$ at C, and $7.94 \times 10^{14} \text{ n cm}^{-2} \text{ s}^{-1}$ at D. We note that all of these fluxes are lower than the $1.04 \times 10^{15} \text{ n cm}^{-2} \text{ s}^{-1}$ total flux calculated for the conceptual power plant model B that was used for the scoping calculations reported in [1] because that was a higher-powered device (3.6 GW of thermal power compared to 3.0 GW) than the one considered here, which explains why the gas concentrations in figure 5 are at least 30% lower than those given there (see table 3 of [1]).

The variation in He and H production rates in Fe (figure 5), particularly between position B, at the top of the vessel, and the other three, appears to be greater than that suggested by comparing the ratios of the total flux in the different FW regions. Both the $^{56}\text{Fe}(n, \alpha)^{53}\text{Cr}$ and $^{56}\text{Fe}(n, p)^{56}\text{Mn}$ reactions, which are responsible for most of the He and H produced in pure Fe, respectively, are threshold reactions. Only for neutron energies above the threshold does a reaction become possible, and for the (n, α) and (n, p) reactions on ^{56}Fe the thresholds are at approximately 3.7 MeV and 2.9 MeV, respectively [14]. From the close examination of the spectra for the different positions it is apparent that at B in figure 2 there is a noticeable reduction in the neutron energies above 1 MeV (see figure 6), which is precisely the range over which the gas production reactions become more likely, and so helium and hydrogen production at B is reduced. After five full-power years, for example, the

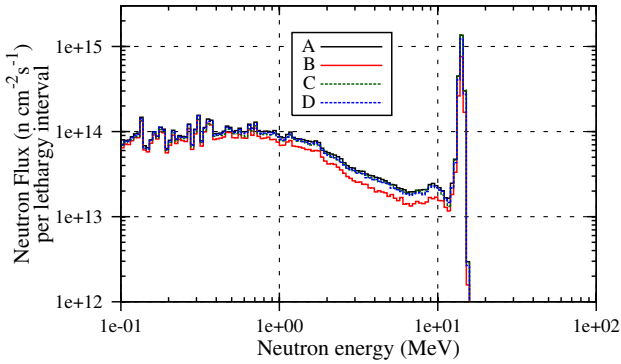


Figure 6. The high-energy part of the neutron spectra for the 2 cm FW armour layer at four different positions within the DEMO model (figure 2). The slight drop in the flux at B shown here leads to the $\sim 50\%$ drop in gas production in figure 5.

He concentration in the FW armour at B has only reached 365 atomic parts per million (appm), while in the FW armour at the other three positions the He concentration after five years is 709 appm, 734 appm and 586 appm for positions A, C, and D, respectively. The reduction in frequency of the threshold reactions at B also accounts for the greatly reduced dpa/year rate in pure Fe—in regions A–C the dpa/year is of the order of 13–14, while at B it is less than 10 dpa year⁻¹.

As a function of depth into the vessel from the plasma at position A we have already seen that neutron-irradiation conditions change dramatically between the plasma-facing wall and the outer edge of the blanket (see figure 3), with the total flux and dpa/year reducing and the energy spectrum becoming softer. Inventory calculations reveal that these changes cause the He (and H) production levels to fall significantly. For example, from the results presented in figure 7 for the He concentration after five full-power years, the He concentration in the FW armour is around 700 appm at A, while in the final 5 cm of the blanket, which is at a total depth from the plasma of 57–62 cm, the amount of He only reaches 3 (three) appm. Over the same range, the dpa rate in pure Fe falls from 14.4 dpa year⁻¹ in the FW armour to only 1 dpa year⁻¹ at the outer edge of the blanket (figure 4). Such a profound change in both gas production and dpa rates could have important consequences in terms of He-induced brittleness in Fe and hence steels.

However, the neutron spectra calculated by MCNP do not take into account time-dependent compositional changes in materials, i.e. each neutron is propagated through the model as though it were the first. For the blanket, in particular, which is solid-type helium-cooled pebble-bed (HCPB) concept in the model, the compositional changes that take place as a result of nuclear reactions could lead to a significant evolution (in time) in the neutron-irradiation conditions. Neutrons entering the blanket are moderated by Be and subsequently absorbed efficiently by Li, in particular ⁶Li, to produce tritium. Initially, this happens predominantly in the first few centimetres of the blanket, leading to the changes in neutron spectrum and flux, and thus gas production, observed in the present calculations. Subsequently, as the Li is burnt-up (transmuted) in these near-plasma regions, fewer of the neutrons are absorbed and so the flux at greater depths can increase in the thermal energy ranges. The cycle then repeats as the Li in deeper regions of

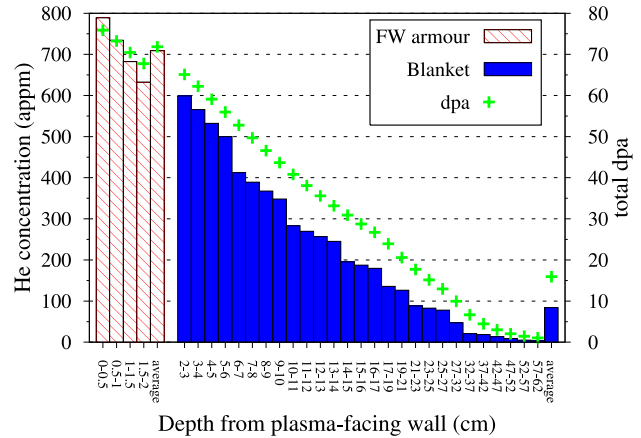


Figure 7. Variation in He concentration in pure Fe after a five-year irradiation as a function of depth (from the plasma) into the FW armour and blanket of DEMO at A in figure 2. The total dpa in pure Fe at each depth after five years is also shown (pluses).

the blanket is depleted, and so on. Hence, it is possible that if this time evolution were taken into account the He-production rates in the near-plasma regions of the blanket would decrease in time as the ⁶Li is depleted, while in the outer regions the He-production rates would increase as the thermal component of the spectrum in these regions rises and more ⁶Li(n,t)⁴He reactions take place. However, the high-energy parts of the neutron spectrum would be largely unaffected by this process and so He-production rates from other elements, such as Be and Fe, where the associated reactions have thresholds, would remain relatively constant, apart from a small reduction caused by the burn-up Be in particular. Such a time evolution can be investigated by coupling MCNP to an inventory code (such as FISPACT), which updates the material compositions in the model at frequent intervals, thus allowing the changes in neutron flux and spectra to be quantified. This method has recently been applied by Packer *et al* [15] to investigate how the tritium-breeding inventory evolves in the DEMO blanket.

Another important observation from figure 7, is that care should be taken when using the spectra averaged over large regions of reactor vessels. While the results for the volume-averaged flux in the FW armour at A are in broad agreement with the finer, 0.5 cm, divisions because the FW armour is only 2 cm thick, for the 60 cm blanket the average is a poor representation, predicting only 84 appm after five years, compared to 600 appm in the first 1 cm of the blanket. The difference between 84 and 600 appm would be measurable as far as the structural properties of Fe (and steels) is concerned—implanted He concentrations in the range of 400 appm are known to cause significantly more pronounced embrittlement of fission neutron-irradiated steels compared to those exposed to fission neutrons alone [16]. Here we note that fission neutrons on their own do not generate appreciable amounts of transmutation gas products in the materials.

2.2.2. W. While W (tungsten) will be present throughout a typical reactor vessel as a part of the composition present in most steels, including around 1.1 wt% in EUROFER steel, it will be used in an almost pure form primarily in the high

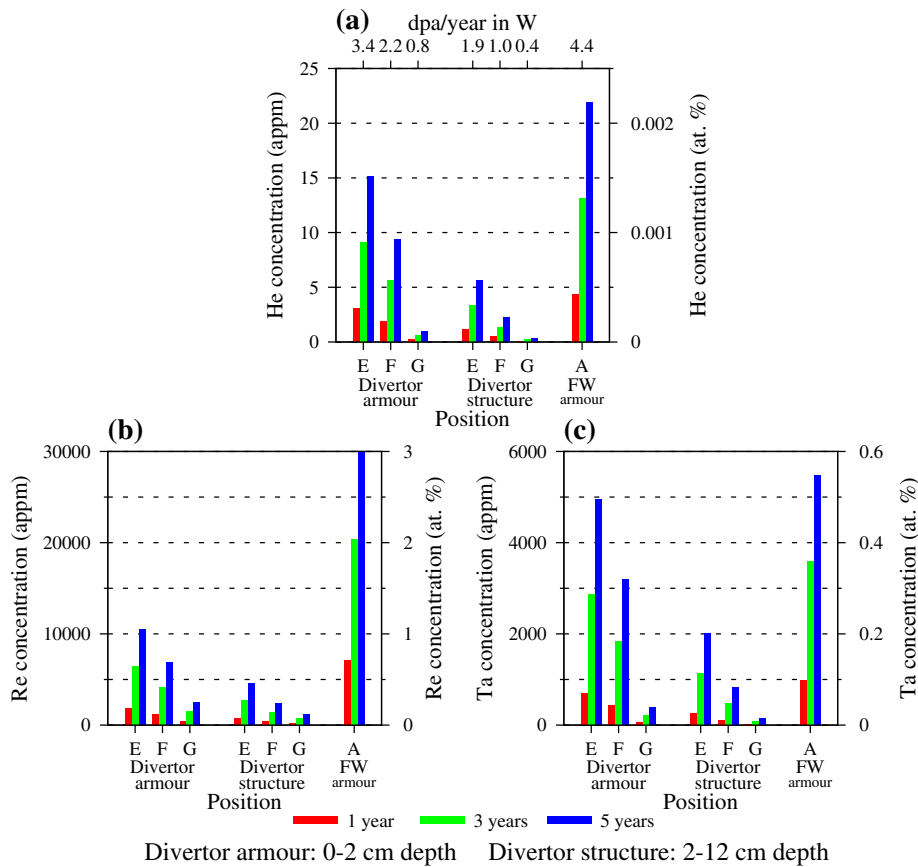


Figure 8. Variation in concentrations of (a) He, (b) Re and (c) Ta, produced in pure W under neutron irradiation as a function of position (and depth) in the divertor region of the DEMO design (figure 2). In (a) the equivalent dpa year⁻¹ in pure W are also given for each position.

heat-flux regions, such as the divertor, because of its high melting temperature, high thermal conductivity, and resistance to sputtering and erosion [17]. In many reactor designs, including the model for DEMO discussed in the present work, it is assumed to be the main material in both the armour and structural components of the divertor, while in some power plant concepts it is also considered for the FW armour layer [2]. As a small part of steels, the transmutation-related gas production from W is unlikely to be consequential, although its transmutation to other elements, such as Re or Os, may cause non-negligible changes in structural properties, but in those regions where W is the chief element, a quantification of gas production is vital.

The results from inventory calculations reveal that the concentration of He produced from pure W can vary significantly, even within the same layer of the divertor. We find that the amount of He produced in the divertor armour (the first 2 cm of the divertor in figure 2) after a five-year full-power irradiation varies from 15 appm at position E, to less than 1 (one) appm at G—an order of magnitude difference—although both could be viewed as negligible. A similar variation with position is also obtained for the 10 cm layer behind the armour (a mixture of W and He, the final 10 cm of the divertor in figure 2). These findings are summarized in figure 8(a). Note that for H, by comparison, the variations with position are of a similar order, although the level of production overall is roughly twice as great as that for He.

Figure 8 also demonstrates that helium production from W is greater in the FW armour than in the divertor. For the present DEMO model, the FW armour layer is very thin, meaning that it is almost transparent to neutrons. Therefore, it is realistic to assume that the fluxes and energy spectra obtained from MCNP calculations with a FW armour of steel on DEMO are very close to those that would be found if the armour were W instead. The observed variation in transmutation response between the FW and the divertor is primarily due to differences in total neutron flux in the FW compared to the divertor, with for example, a flux of $8.25 \times 10^{14} \text{ n cm}^{-2} \text{ s}^{-1}$ in the 2 cm armour at A producing 4.4 dpa year⁻¹ versus $7.51 \times 10^{14} \text{ n cm}^{-2} \text{ s}^{-1}$ giving 3.4 dpa year⁻¹ in the divertor armour at E. However, the variation in shape of the neutron spectra is also a contributing factor. Comparing figures 3(a) and (b), we see that flux levels in the few MeV range are significantly lower in the divertor, which is precisely the region of the energy spectrum that contributes to many of the threshold gas-producing reactions on isotopes of W.

Similarly there are significant reductions in Re concentration between the FW and the divertor (figure 8(b)). After five years in the FW armour at A, Re (rhenium) reaches a concentration of 30 000 appm (3 at%), which is broadly in line with the findings for the FW of PPCS-B in [1] after taking into account the reduction in total flux. However, in the divertor armour at position E, Re only reaches a concentration of around 10 000 appm (1 at%) on the same timescale. This factor of

three reduction is much greater than the ~ 1.1 ratio between the total fluxes in the FW and divertor.

The primary reactions contributing to the production of Re, or heavier elements such as Os, from W are the (n,γ) reactions, which normally have a cross section that is proportional to $1/\sqrt{E_n}$ at low neutron energies E_n . In figure 3 the spectra associated with the divertor regions of the DEMO model have a profile that is much less moderated than that in the FW, which has a large contribution from moderated neutrons that have back-scattered from the Be/Li blanket. Thus, the proportion of neutrons at the lower energies is reduced in the divertor, which leads to a smaller probability for the (n,γ) reactions (compared to other nuclear reactions), and so the production of Re is disproportionately lower.

On the other hand, figure 8(c) suggests that the changes in energy-spectrum profile between the FW and divertor do not particularly alter the rate at which W transmutes into Ta (tantalum). In the armour at location A, the Ta concentration is calculated to be 5470 appm after a five-year exposure, while in the divertor armour at E it is 4940 appm. The ratio between these two values is exactly the same as the ratios of the total flux (~ 1.1), suggesting that this is the main reason for the variation, despite the apparent differences in the energy spectra shown in figure 3.

This is somewhat surprising because many of the nuclear reactions on W that produce Ta, either directly or indirectly, including the $(n,2n)$ reaction on ^{182}W , have thresholds. Based on the high-energy regions of the spectra in figure 3, one might expect these threshold reactions to be reduced in the divertor, leading to a reduction in Ta production compared to the FW armour that is greater than a simple scaling of the total fluxes. However, the average neutron energies associated with the spectra in the armour layers at A and E are quite similar (2.23 MeV versus 1.83 MeV, respectively) suggesting a proportional reduction of neutrons at all energies in the divertor and thus the 1.1 flux-factor difference in Ta production. On the other hand, this then contradicts our explanation above for the changes in Re production, although we have not considered the fact that the two spectra have similar fluxes in the 0.1–1 MeV range. Further investigation is needed to fully quantify these subtle complexities associated with neutron-transport and inventory calculations of this kind.

2.2.3. Be. Beryllium, as the primary constituent of the blanket in the present DEMO model, has been found previously [1] to produce significant concentrations of He under neutron irradiation. For the present model, the inventory calculations indicate He concentrations in Be after five-year irradiations of between 19 300 appm in the first 1 cm of the equatorial blanket at position A in figure 2, to only 200 appm in the final 5 cm (see figure 9). As noted previously, this extreme range of values, which is even greater than the drop observed for Fe in figure 7, is likely to be time-dependent because the neutron-energy spectrum in different regions of the blanket will evolve as the Li is depleted. However, the large difference, which on shorter timescales equates to approximately 320 appm He per month within the inner 1 cm of blanket, and around 3 appm per month in the outer 5 cm, is likely to produce non-homogeneous

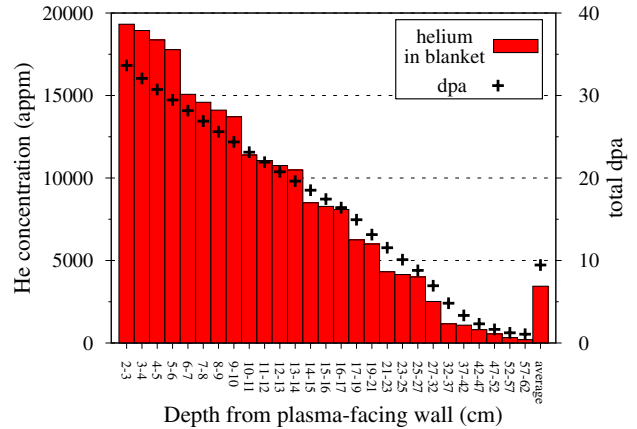


Figure 9. Variation in He concentration in pure Be after a five-year irradiation as a function of depth into the DEMO blanket at (A) in figure 2. The equivalent dpa in pure Be after five years is also given at each depth.

changes to structural and mechanical properties across the full depth of the blanket. For instance, Be is known to swell significantly under neutron irradiation, due to the generation of helium in the bulk of the material [18, 19], and a variation in swelling rates would produce significant stress differentials in components.

Note that, by comparison, hydrogen gas production in Be is around two orders of magnitude less than for He, with, for example, only 475 appm produced in five years of reactor operation under the conditions calculated for the first centimetre of the DEMO blanket at A.

3. Modelling of He accumulation at grain boundaries

The calculations described in the foregoing section produce quantitative estimates of the He-production rates under any neutron-irradiation conditions. However, without knowing what determines the critical concentration of He in a material, it is difficult to fully appreciate the mechanical or structural consequences (or the absence of those) of a particular level of He accumulation. It appears that by applying some straightforward concepts and simplifying assumptions, it is possible to give a conservative estimate for the critical He densities in grains that could lead to the grain-boundary destabilization giving rise to helium embrittlement. Subsequently, the timescales required to produce these densities can be evaluated using the neutron transport and inventory calculations, thus giving insight into the differences in component lifetime caused by grain-boundary embrittlement in different materials.

Assuming that all the crystal grains in the material have cubic shape, we find the total number of He atoms N_{He} within a grain of linear size a as

$$N_{\text{He}} \approx a^3 n G_{\text{He}}, \quad (4)$$

where G_{He} is the atomic concentration of He atoms produced through transmutation reactions, and n is the atomic density of the material (cm^{-3}), which for a given material are evaluated using atomic weights and mass densities (see table 1). If every

He atom produced in a grain is able to migrate to the boundaries of the grain, then ν_{He} , the surface density of He at the grain boundary (GB), satisfies

$$3a^2\nu_{\text{He}} = a^3nG_{\text{He}},$$

where in a lattice of cubic grains helium produced in each grain can be attributed to the three of its boundaries (the other boundaries receive He from neighbouring grains). Therefore,

$$\nu_{\text{He}} = \frac{a}{3}nG_{\text{He}}. \quad (5)$$

In a real material the evolution of microstructure under irradiation would give rise to the formation of internal obstacles, such as dislocations and vacancy clusters, that will trap some of the He atoms in the bulk of the grain, preventing them from reaching the grain boundaries. Traps may also be introduced artificially during processing of the material, for example in the form of nano-scale oxide particles [20]. The presence of such traps is neglected here for simplicity. Consequently, the predictions based on this model can be considered as representing conservative *worst-case* scenarios for He-induced grain-boundary embrittlement.

The grain structure of a material destabilizes (i.e. the grain boundaries split apart and the material fails) if the stored energy associated with He accumulated at boundaries becomes greater than or equal to the energy required to make all the boundaries become free surfaces. If we now approximate the energy of solution of a He atom at a boundary by the energy of solution for a He atom *at a substitutional site* in a perfect lattice $E_{\text{He}}^{\text{sol}}$, then

$$E_{\text{He}}^{\text{sol}}\nu_{\text{He}}^{\text{c}} \approx 2\varepsilon_{\text{surf}}, \quad (6)$$

where $\varepsilon_{\text{surf}}$ is the surface energy per unit area for the given material, which is multiplied by two here because each GB is associated with two grains. Whereas it is conceivable that at certain boundaries, corresponding to particular orientations of neighbouring grains, the configuration adopted by He atoms may be more favourable than in the grain bulk, it is likely that our estimate for the energy of solution, evaluated using electronic-structure based methods for helium atoms occupying vacancy sites in a lattice, are fairly close to the energy of solution of helium atoms at grain boundaries. Hence the above defined quantity $\nu_{\text{He}}^{\text{c}}$ is very close to the actual critical surface density of He atoms required to bring-about boundary destabilization. Once $\nu_{\text{He}}^{\text{c}}$ is known, the critical bulk He concentration G_{He}^{c} is readily found from equation (5):

$$G_{\text{He}}^{\text{c}} = 3\nu_{\text{He}}^{\text{c}}/an. \quad (7)$$

Table 2 shows the values of $\nu_{\text{He}}^{\text{c}}$ and G_{He}^{c} calculated for various elemental metals considered as candidate materials for fusion applications. To find these values we have used the estimates of surface and He-solution energies given in table 1. Since we do not know the specific grain orientations associated with fracture, the values of surface energy given in the table are estimated as the average of experimental values reported by Vitos *et al* [26]. Similarly, for the He-solution energies, we have taken the values found using first-principles electronic-structure calculations performed using density functional theory (DFT) for the substitutional position of a He atom in the lattice from [22–25].

Table 1. Table of basic quantities used for evaluating critical helium grain-boundary concentrations giving rise to the loss of structural integrity of components. ρ^{RT} is the density of the material at room temperature (RT), n is the atomic density (see equation (5)), $E_{\text{He}}^{\text{sol}}$ is the solution energy of a He atom at a substitutional site, and $\varepsilon_{\text{surf}}$ is the average surface energy.

Element	ρ^{RT} (g cm ⁻³) ^a	Atomic mass (amu) ^a	n (cm ⁻³)	$E_{\text{He}}^{\text{sol}}$ (eV)	$\varepsilon_{\text{surf}}$ (Jm ⁻²) ^e
Fe	7.87	55.845	8.5×10^{22}	4.34 ^b	2.4
V	6.11	50.942	7.2×10^{22}	4.81 ^b	2.6
Cr	7.19	51.996	8.3×10^{22}	5.20 ^b	2.3
Mo	10.22	95.940	6.4×10^{22}	4.65 ^b	3.0
Nb	8.57	92.906	5.6×10^{22}	4.55 ^b	2.7
Ta	16.65	180.948	5.5×10^{22}	4.82 ^b	3.0
W	19.25	183.840	6.3×10^{22}	4.77 ^b	3.5
Be	1.85	9.012	1.2×10^{23}	3.46 ^c	2.2
Zr	6.51	91.224	4.3×10^{22}	3.08 ^d	2.0

^a Data taken from [21].

^b DFT result from [22].

^c DFT result from [23, 24].

^d DFT result for interstitial configuration from [25].

^e Averages of experimental values reported in [26].

Here it is appropriate to consider the validity of the model formulated above. Despite its apparent simplicity, our critical boundary densities appear to be in reasonable agreement with experiment. For example, in experiments performed by Gerasimenko *et al* [27] bicrystalline W was bombarded with relatively low-energy helium ions, resulting in the accumulation of helium at grain boundaries and sudden increase in grain-boundary width observed at certain critical ion fluxes in the range 10^{14} – 10^{15} ions cm⁻², which is exactly the range into which our estimate for grain-boundary failure in W (and in other materials) falls. In fact, considering figure 1 in [27], we note that our estimate is slightly higher, which can be explained by removing the assumption that the He atoms form a uniform layer across the entire interfacial area of a grain—in reality, the He will preferentially segregate at pre-existing sites at the interface leading to enhanced destabilization and lower critical boundary densities.

We should note that it may also be possible to give a more accurate assessment of grain-boundary embrittlement because of recent developments in large-scale density functional calculations, where not only individual helium defects but also the structure of helium clusters can be explored using predictive mathematical models [28–30]. These models show that helium atoms are readily trapped by the vacancies that are produced both thermally and by the irradiation itself. Also, helium atoms form strongly self-bound clusters that can nucleate spontaneously in a perfect crystal lattice and on helium atoms initially trapped by vacancies [28, 30]. The effect of formation of small helium clusters is likely responsible for the behaviour, observed in experiments on irradiated beryllium [31], where large visible bubbles of helium formed once the specimens were heated to temperatures in excess of 600 °C. Such helium clustering effects can in principle be included in a more accurate microstructural-evolution-based model for helium accumulation and embrittlement of components in a fusion power plant.

The G_{He}^{c} values in table 2 show significant variation between different elements. Note that G_{He}^{c} , as defined here, is strongly dependent on the parameters $E_{\text{He}}^{\text{sol}}$, $\varepsilon_{\text{surf}}$, and n , and so

Table 2. Table of calculated critical boundary densities v_{He}^c , critical bulk concentrations G_{He}^c for He in various elements, and the approximate critical embrittlement-lifetimes t^c in DEMO full-power time and equivalent integral dpa. Results for two different grain sizes a shown.

Element	v_{He}^c (cm^{-2})	a (μm)	G_{He}^c (appm)	Critical times and dpa for GB embrittlement in DEMO			
				FW armour		blanket at depth of 17–19 cm	
				t^c	dpa ^c	t^c	dpa ^c
Fe	6.90×10^{14}	5	48.8	4 months	4.79	2 years	9.57
V	6.75×10^{14}	5	56.1	1.5 years	25.07	7 years	41.52
Cr	5.52×10^{14}	5	39.8	5 months	6.27	2.5 years	12.75
Mo	8.05×10^{14}	5	75.3	2 years	19.12	10 years	31.26
Nb	7.41×10^{14}	5	80.0	2 years	31.99	10 years	51.61
Ta	7.77×10^{14}	5	84.1	19 years	107.60	137 years	304.17
W	9.16×10^{14}	5	87.2	20 years	88.89	228 years	357.37
Be	7.94×10^{14}	5	38.5	4 days	0.08	11 days	0.09
Zr	8.11×10^{14}	5	113.2	4 years	61.99	21 years	108.80
Fe	6.90×10^{14}	0.5	488.0	4 years	57.47	18 years	86.13
V	6.75×10^{14}	0.5	560.5	12 years	200.60	69 years	409.29
Cr	5.53×10^{14}	0.5	397.8	4 years	60.20	23 years	117.34
Mo	8.05×10^{14}	0.5	753.2	18 years	172.10	114 years	356.42
Nb	7.41×10^{14}	0.5	800.1	17 years	271.94	100 years	516.12
Ta	7.77×10^{14}	0.5	841.3	216 years	1223.20	> 300 years	>666.00
W	9.16×10^{14}	0.5	871.5	>300 years	>1333.00	>300 years	>470.00
Be	7.94×10^{14}	0.5	385.2	1 month	0.60	4 months	1.00
Zr	8.11×10^{14}	0.5	1131.7	37 years	573.39	217 years	1124.29

refinement of the approximate values for these quantities might significantly alter the embrittlement-lifetime predictions.

Even though Zr (zirconium) has the lowest He-solution energy (3.08 eV), it also has a relatively low atomic density, leading to the greatest critical bulk He concentration G_{He}^c because $G_{\text{He}}^c \propto 1/n$. Be, on the other hand, has the highest atomic density n , and so, unsurprisingly, has the lowest G_{He}^c value and is likely to be more susceptible than most to He-induced grain-boundary embrittlement.

With these G_{He}^c values we can now estimate the time taken to produce these critical He concentration at grain boundaries under neutron irradiation. To allow a direct comparison between different materials, the critical embrittlement-lifetimes t^c and equivalent integral values of NRT dpa given in table 2 were computed for identical irradiation conditions in each case. Here we have used two characteristic irradiation conditions from the MCNP neutron-transport calculations for the outboard equatorial FW at A in figure 2: the result for the 2 cm FW armour, which has a total neutron flux of $8.25 \times 10^{14} \text{ n cm}^{-2} \text{ s}^{-1}$; and the conditions for the blanket at a depth of 17–19 cm, which has a total flux of $4.35 \times 10^{14} \text{ n cm}^{-2} \text{ s}^{-1}$. Note that in the case of inventory calculations, there is not necessarily a linear relation between the G_{He}^c and t^c , because of the subtleties associated with transmutation. For instance, as an element is burnt-up, the products may be more (or less) prone to He production, leading to an acceleration (or deceleration) in accumulation as time progresses.

Beryllium, with its low critical density G_{He}^c and high He-production rates, has the lowest estimated lifetimes and dpa before embrittlement; the predicted t^c for a grain size of $5 \mu\text{m}$ is only 4 days, corresponding to 0.08 dpa, under the equatorial outboard FW armour conditions, and even at depth of ~ 20 cm into the blanket t^c is only 11 days for the same grain size. Meanwhile W and Ta have high critical densities

and low He-production rates, implying long embrittlement-lifetimes; more than 200 years and 1000 dpa in the FW armour for the small $0.5 \mu\text{m}$ grains. Even for the large, $5 \mu\text{m}$ grains, the predicted t^c for W is 20 years or 89 dpa for the FW armour and more than 200 years at 17–19 cm in the blanket, suggesting that, even under FW conditions, the issue of He embrittlement might not be a cause for concern. On the other hand, Mo, which could conceivably be an alternative to W as a divertor or FW armour material, has much higher He-production rates, so the predicted t^c s, at 2 years and 18 years for the large and small grains, respectively, in the FW armour are much shorter, even though the required G_{He}^c are similar to those in W.

More crucially, however, the FW armour t^c s predicted for the two grain sizes in Fe go from the problematic at 4 months or 5 dpa for a $5 \mu\text{m}$ grain, to commercially viable at 4 years (recent estimates put a commercially viable lifetime of 5 years in the FW of a power plant [32]) or 57 dpa in the limit of small, $0.5 \mu\text{m}$ grains, where our assumption of no traps is most valid. Similarly, the t^c value for Fe in the 17–19 cm blanket region is only 2 years for the larger grain size, but comfortable at 18 years when $a = 0.5 \mu\text{m}$. This illustrates how critical material grain size might be in defining the lifetime of fusion-reactor components.

Here we would like to highlight the fact that our estimates for the critical helium concentrations for a $0.5 \mu\text{m}$ grain size are in broad agreement with experimental data by Yamamoto *et al*, see figure 1 of [16], who found evidence of significant helium-mediated grain-boundary embrittlement of ferritic–martensitic steels occurring once the concentration of helium in the bulk of the grain approached ~ 500 appm.

This shows that despite the roughness of the approximations made in the preceding arguments, the results are able to demonstrate that materials exposed to high neutron fluxes and energies can exhibit vastly differing evolution in properties (in this case grain-boundary embrittlement) over their

period of service. Further work in this area, including investigations of the influence of He traps (such as dislocations and voids), which can cause swelling, interaction with hydrogen, preferential accumulation, and temperature effects, are needed to provide accurate predictions of He-embrittlement-limited component lifetimes. The present work is a first step in this investigation, and, despite the *worst-case* scenarios envisaged in the modelling, demonstrates the possibility of linking neutron-transport and inventory calculations to engineering relevant mechanical properties.

4. Summary

The combined MCNP-based neutron-transport simulations and FISPACT-based inventory calculations for the neutron-irradiation conditions expected in the DEMO concept reactor demonstrate that He accumulation rates, and transmutation rates in general, can vary dramatically, even within the same component of a fusion reactor. In Fe, the production of He is likely to be significant and severe within the first wall armour of a reactor, but will fall off rapidly in deeper radial locations, through the tritium-breeding blanket, due to the effective moderation and absorption of neutrons required for efficient production of tritium (^3H). By the time neutrons reach the outer vessel components, such as the shield and vacuum-vessel walls, the quantities of He predicted are at such a low level that they are unlikely to pose a serious threat to the structural integrity of components.

In W the predicted He concentrations are probably too low to have any impact on component lifetime, and it is more likely that the build-up of defects due to neutron-irradiation cascades, leading to hardening and embrittlement, will be the life-limiting mechanism for W-based materials. In this respect, further work is needed to assess the acceptable levels of other transmutation products in W, such as Re, Ta and Os, because these can reach non-negligible levels, and might influence the evolution of radiation damage, causing both desirable and undesirable changes to mechanical properties.

In Be, on the other hand, the inventory calculations confirm the previous findings [1], and show that He can be produced in significant quantities, particularly in the inner, near-plasma regions of the blanket, which, in turn, produces very-short predictions of embrittlement-lifetime. Perhaps more concerning are the implications associated with inhomogeneous swelling rates in the same blanket component caused by the two orders of magnitude difference between the initial He-production rates at the inner and outer edges of blanket components.

However, as noted, this could vary in time as the Li in the tritium-breeding blanket is depleted, reducing the neutron absorption rate. Eventually, as the DEMO design is refined and finalized, fully fledged fuel-cycle calculations of inventory burn-up will be needed to complement and improve not only the findings for Be, but additionally for other materials, whose burn-up will also be strongly influenced by the changing environment within the blanket.

The basic modelling of the He-induced grain-boundary embrittlement of various different candidate fusion materials reveals that the range of expected critical embrittlement-lifetimes before grain boundaries would begin to destabilize

might vary greatly as a function of the particular materials (elements) chosen, as well as a function of position within a specific reactor design. For instance, structural Fe, under suitable conditions, may adequately withstand He embrittlement on commercially viable timescales, even in the plasma-exposed first wall armour. However, Be almost certainly would not, unless a way can be found to mitigate the swelling and embrittlement caused by the vast quantities of He it produces under neutron irradiation.

On their own, the different computational techniques applied in this work only give a narrow view of the conditions and processes that take place within materials under fusion-neutron irradiation. However, by linking them together and using the predictions from one to inform the predictions in another, we have shown that it is possible to develop a fuller appreciation of the consequences for real mechanical properties caused by the variation in the nuclear environment within a fusion power plant.

Acknowledgments

The authors gratefully acknowledge helpful discussions with R.G. Odette, M. Rieth, T. Yamamoto, D. Nguyen-Manh and P. Karditsas. This work, partly funded by the European Communities under the contract of association between EURATOM and CCFE, was carried out within the framework of the European Fusion Development Agreement. The views and opinions expressed herein do not necessarily reflect those of the European Commission. This work was also part-funded by the RCUK Energy Programme under Grant No EP/I501045. S.L. Dudarev would like to acknowledge support from the EURATOM staff mobility program.

© Euratom 2012.

References

- [1] Gilbert M.R. and Sublet J.-Ch. 2011 *Nucl. Fusion* **51** 043005
- [2] Maisonnier D. *et al* 2005 *Fusion Eng. Des.* **75–79** 1173–9
- [3] Pampin R. and Karditsas P.J. 2006 *Fusion Eng. Des.* **81** 1231–7
- [4] Karditsas P.J. 2008 *Fusion Eng. Des.* **83** 1638–42
- [5] Brown F.B. *et al* 2002 *Trans. Am. Nucl. Soc.* **87** 273–6
- [6] Rieth M., Klimenkov M., Materna-Morris E. and Möslang A. Review of the physical metallurgy of EUROFER 2008; *Final Report EFDA task TW6-TTMS-007 D10*
- [7] MacFarlane R.E. and Muir D.W. 1994 The NJOY Nuclear Data Processing System: Version 91; LA-12740-M (UC-413), Los Alamos National Laboratory Report, October 1994
- [8] Ougouag A.M., Wemple C.A. and Van Siclen C.D. 2004 Displacement Kerma Cross Sections For Neutron Interactions In Molybdenum; INEEL/CON-03-01258, Idaho National Engineering and Environmental Laboratory, April 2004
- [9] Lindhard J., Nielsen V., Scharff M. and Thomsen P.V. 1963 *Mat. Fys. Medd. Dan. Vid. Selsk.* **33** 1–42
- [10] Norgett M.J., Robinson M.T. and Torrens I.M. 1975 *Nucl. Eng. Des.* **33** 50–4
- [11] Panini G.C. and Peerani P. 1991 A Library of Nuclear Response Functions in Vitamin-J Structure; RFL-1, presented at the *EFF Meeting, NEA Data Bank, (Saclay, Paris, France, December 1991)* www.oecd-nea.org/html/dbdata/nds_effdoc/effdoc-130.pdf
- [12] Stoller R.E., Calder A.F., Osetsky Yu.N. and Bacon D.J. 2011 Displacement cascade evolution: neutron irradiation versus ion near-surface damage *Presentation given at the*

- Workshop on Ion Implantation as a Neutron Irradiation Analogue (Oxford, UK, September 2011)* (unpublished) <http://mffp.materials.ox.ac.uk/content/workshop-ion-implantation-neutron-irradiation-analogue>
- [13] Forrest R.A. 2007 FISPACT-2007: User manual, UKAEA FUS 534
- [14] Forrest R.A. 2002 The European Activation File: EAF-2003 overview, UKAEA FUS 484
- [15] Packer L.W., Pampin R. and Zheng S. 2011 *J. Nucl. Mater.* **417** 718–22
- [16] Yamamoto T., Odette G.R., Kishimoto H., Rensman J.W. and Miao P. 2006 *J. Nucl. Mater.* **356** 27–49
- [17] Nemoto Y., Hasegawa A., Satou M. and Abe K. 2000 *J. Nucl. Mater.* **283–287** 1144–7
- [18] Chakin V.P., Posevin A.O. and Kupriyanov I.B. 2007 *J. Nucl. Mater.* **367–370** 1377–81
- [19] Möslang A., Pieritz R.A., Boller E. and Ferrero C. 2009 *J. Nucl. Mater.* **386–388** 1052–5
- [20] Hsiung L.L., Fluss M.J., Tumey S.J., Choi B.W., Serruys Y., Willaime F. and Kimura A. 2010 *Phys. Rev. B* **82** 184103
- [21] Lide D.R. (ed) 2004 *CRC Handbook of Chemistry and Physics* 85th edn (Boca Raton, FL: CRC Press)
- [22] Willaime F. and Fu C.C. 2006 *Mater. Res. Soc. Symp.* **981** 0981-JJ05-04
- [23] Ganchenkova M.G., Vladimirov P.V. and Borodin V.A. 2009 *J. Nucl. Mater.* **386–388** 79–81
- [24] Middleburgh S.C. and Grimes R.W. 2011 *Acta Mater.* **59** 7095–103
- [25] Koroteev Yu.M., Lopatina O.V. and Chernov I.P. 2009 *Phys. Solid State* **51** 1600–7
- [26] Vitos L., Ruban A., Skriver H. and Kollár J. 1998 *Surf. Sci.* **411** 186–202
- [27] Gerasimenko V.I., Mikhaïlovskii I.M., Neklyudov I.M., Parkhomenko A.A. and Velikodnaya O.A. 1998 *Tech. Phys.* **43** 803–8
- [28] Becquart C.S. and Domain C. 2006 *Phys. Rev. Lett.* **97** 196402
- [29] Fu C.C. and Willaime F. 2005 *Phys. Rev. B* **72** 064117
- [30] Fu C.C. and Willaime F. 2007 *J. Nucl. Mater.* **367–370** 244–50
- [31] Andreev D.V., Bespalov V.N., Birjukov A.Y., Gurovich B.A. and Platonov P.A. 1996 *J. Nucl. Mater.* **233–237** 880–5
- [32] Maisonnier D., Cook I., Sardain P., Boccaccini L., De Pace L., Giancarli L., Norajitra P. and Pizzuto A. 2006 *Fusion Eng. Des.* **81** 1123–30